

Fast dynamic aperture optimization with reversal integration

Yongjun Li,^{1,*} Yue Hao,² Kilean Hwang,³ Robert Rainer,¹ An He,¹ and Ao Liu⁴

¹*Brookhaven National Laboratory, Upton, New York 11973, USA*

²*FRIB/NSCL, Michigan State University, East Lansing, Michigan 48864, USA*

³*Lawrence Berkeley National Laboratory, Berkeley 94720, California, USA*

⁴*Euclid Techlabs, LLC, Bolingbrook, Illinois 60440, USA*

A fast method for dynamic aperture (DA) optimization of storage rings has been developed through the use of reversal integration. While chaotic dynamical systems have exact time-reversal symmetry, numerical forward integration differs from its reversal due to scaled cumulative round-off errors. The difference, intrinsically associated with the Lyapunov exponent, is a generic indicator of chaos because it represents the sensitivity of chaotic motion to an initial condition. A chaos indicator of the charged particle motion is then obtained by comparing the forward integrations of particle trajectories with corresponding reversals, a.k.a. “backward integrations.” The indicator was confirmed to be observable through short-term particle tracking simulations. Therefore, adopting it as an objective function could speed up optimization. The DA of the National Synchrotron Light Source II storage ring, and another test diffraction-limited light source ring, were optimized using this method for the purpose of demonstration.

I. INTRODUCTION

Accurate computation of the Lyapunov exponent (LE) of particle motion in accelerators and comparison with numerical dynamic aperture (DA) simulations has been well studied. Past examples include [1?–5]. A general correlation between the LE and the DA has been confirmed, but a universal or quantitative equivalence has yet to be established. In some studies, the LE was found to underestimate the chaos of particle trajectories in storage rings [5]. Additionally, accurate calculation of the LE [2, 6] is time-consuming due to the long-term numerical integrations required, making its use difficult in direct dynamic aperture optimization.

The discovery of another indicator of chaos, obtained by comparing forward integrations and corresponding reversals (i.e. backward integration), can be traced back to the 1950’s [7]. The method is also known as “the trajectory reversing method”, and has been widely used to estimate stable regions of dynamical systems since then [8–13]. One of the more recent uses of this indicator has been to understand the DA of the Integrable Optics Test Accelerator (IOTA) in the presence of space charges [14]. The indicator is intrinsically associated with the LE, because it also represents the sensitivity of chaotic motion to an initial condition. We found that implementing just a few iterations of forward-reversal (F-R) integrations reveal an observable difference using high precision (e.g. 64-bit) floating point numbers for modern storage rings. Therefore, the chaos indicator can be computed at a faster rate. By combining population-based optimization, such as multi-objective genetic algorithm (MOGA) [15–22] with the trajectory reversing method, a fast approach for DA optimization has been developed and demonstrated with two examples in this paper.

Tracking-based optimization has traditionally been limited by time-consuming tracking simulations. The new approach provides a potential solution to using short-term tracking simulations to optimize the DA for large scale storage rings.

To further explain this approach, the remaining sections are outlined as follows: Sect. II briefly explains the F-R integration as an indicator of chaos. A Hénon map’s chaos is studied with this method in Sect. III. In Sect. IV, we take the National Synchrotron Light Source II (NSLS-II) storage ring and another test diffraction-limited light source ring as two examples to demonstrate the proof of concept of this approach. A brief summary is given in Sect. V.

II. FORWARD-REVERSAL (F-R) INTEGRATIONS

In dynamical systems, the Lyapunov exponent (LE) is used to characterize the rate of separation of two infinitesimally close trajectories. In phase space, two trajectories with initial separation $\Delta\mathbf{z}(0)$ diverge at a rate given by,

$$|\Delta\mathbf{z}(t)| = e^{\lambda t} |\Delta\mathbf{z}(0)|, \quad (1)$$

where, $\mathbf{z}(t) = (x, p_x; y, p_y; s, p_s)_t$ is a vector composed of canonical coordinates in phase space at time t , and λ is the LE. Bold symbols, such as “ \mathbf{z} ”, are used to denote vectors throughout this paper. The above rate calculation assumes the divergence is treated as a linearized approximation. The rate of separation can be different for different orientations of the initial separation vector, which yields multiple LEs for a given dynamical system. The largest LE of a system is referred to as the maximal Lyapunov exponent (MLE). The MLE can be defined as,

$$\lambda = \lim_{t \rightarrow \infty} \lim_{\Delta\mathbf{z}(0) \rightarrow 0} \frac{1}{t} \ln \frac{|\Delta\mathbf{z}(t)|}{|\Delta\mathbf{z}(0)|}. \quad (2)$$

* Email: yli@bnl.gov

The MLE provides valuable information about the dynamical system's predictability. $\Delta z(0) \rightarrow 0$ ensures the validity of the linear approximation at any given time. In accelerators, it is more practical to use the path length of a reference particle s rather than time t as the free variable. The trajectory of an arbitrary particle can therefore be described as a deviation from the reference particle. For example, the momentum offset can be denoted as $\delta = \frac{\Delta p}{p_0}$. After some canonical transformations [23], the time t -integration can be converted to a path length s -integration. A new LE λ_s can then be re-defined as,

$$\lambda_s = \lim_{s \rightarrow \infty} \lim_{\Delta z(0) \rightarrow 0} \frac{1}{s} \ln \frac{|\Delta z(s)|}{|\Delta z(0)|}, \quad (3)$$

where $z(t) = (x, p_x; y, p_y; s - ct, \delta)_s$ are 6 new canonical coordinates in the phase space at position s , and $s - ct$ is the longitudinal coordinate offset. For convenience, the rest of this manuscript will use path length s of particle motion as the free variable unless stated otherwise.

Generally speaking, the calculation of LEs as defined above in Eq. (2)-(3), often cannot be carried out analytically. In these cases the calculation would therefore require the use of numerical techniques [2, 6]. An alternative, empirical method to measure the chaos of a dynamical system is to use a reversal integration as suggested in Ref. [7, 8, 14]. During proof of concept, the properties of the system under time symmetry were calculated by letting the system evolve through some number of integration steps, then switching the sign of the time step and letting the system run backward until the total time variable reached zero. On the return to time zero, the changes in corresponding velocities and positions were calculated and collated, as was the value of the time variable during the change of sign. A new set of initial conditions could then be re-established. Due to the unavoidable numerical round-off error [24, 25], the re-established initial conditions deviated from the original ones as illustrated in Fig. 1. The difference, a.k.a. the consistence error, is an indicator of chaos which is associated with its LE.

The principle of the F-R integration approach can be briefly outlined as follows: A nonlinear transfer function, denoted as f , propagates through an N -dimensional phase space coordinate $z = (x_1, x_2, \dots, x_N; p_1, p_2, \dots, p_D)^T$ iteratively. The superscript (T) represents the transpose of a vector. In a finite-precision computation process, the iteration from the $(n-1)$ th state z_{n-1} to the next state z_n reads as:

$$z_n = f(z_{n-1}) + \Delta z_n. \quad (4)$$

where $\Delta z_n = (\Delta x_1, \dots, \Delta x_N; \Delta p_1, \dots, \Delta p_N)^T$ is the round-off error vector when performing the n th iteration. The reversal integration can similarly be written as,

$$z'_{n-1} = f^{-1}(z'_n) + \Delta z'_n, \quad (5)$$

where, f^{-1} is the inverse map, and primes ($'$) denote the coordinates of the reversal so as to distinguish from the

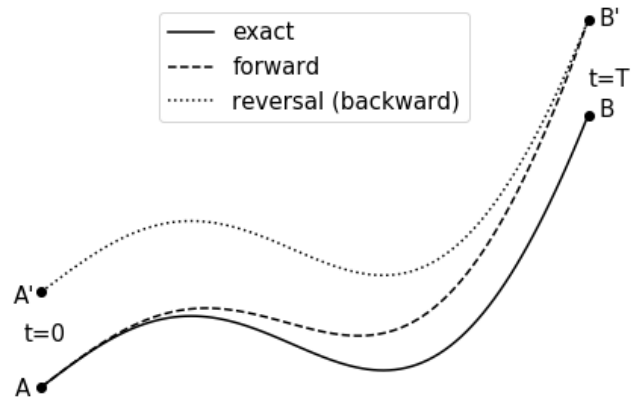


Figure 1. Schematic illustration of forward and time-reversal integrations for a dynamical system. The solid line represents the exact trajectory from A at $t = 0$ to B at $t = T$. The dashed line is the numerical integration, which becomes B' at $t = T$. The difference between B and B' indicates the chaos, but in practice, B is usually unknown. The dotted line is the time-reversal integration starting from B' and ending at A' . The difference between two initial conditions A and A' is an indicator of chaos of the system for this specific initial condition.

forward trajectory. The errors Δz , $\Delta z'$ are distributed uniformly and randomly within a range determined by the values of z , z' , and the number of bits of the computation unit [24]. Modern computers with 64 bit processors are capable of restricting the magnitudes of the round-off errors to much less than that of the values in the vectors,

$$|\Delta z_n| / |z_n| \ll 1, \quad |\Delta z'_n| / |z'_n| \ll 1. \quad (6)$$

When considering a case in which only one F-R iteration is computed, $z_0 \xrightarrow{f} z_1 \xrightarrow{f^{-1}} z'_0$. The difference between z_0 and z'_0 can be estimated with local linear derivatives,

$$\begin{aligned} z'_0 - z_0 &= f^{-1}(f(z_0) + \Delta z_1) + \Delta z'_1 - z_0 \\ &\approx \left. \frac{\partial f^{-1}}{\partial z} \right|_{f(z_0)} \Delta z_1 + \Delta z'_1 \\ &= \left[\left. \frac{\partial f}{\partial z} \right|_{z_0} \right]^{-1} \Delta z_1 + \Delta z'_1, \end{aligned} \quad (7)$$

where the inverse Jacobian matrix of f is evaluated at z_0 . For the sake of simplicity, the linearized matrix for 1-dimension x - p is shown as,

$$\left[\left. \frac{\partial f}{\partial z} \right|_{z_0} \right]^{-1} = \begin{bmatrix} \frac{\partial x_n}{\partial x_{n-1}} & \frac{\partial x_n}{\partial p_{n-1}} \\ \frac{\partial p_n}{\partial x_{n-1}} & \frac{\partial p_n}{\partial p_{n-1}} \end{bmatrix}^{-1}. \quad (8)$$

Eq. (7) indicates that the difference $|z'_0 - z_0|$ originates from random round-off errors, which are scaled by an inverse Jacobian matrix Eq. (8) on the passage of z_0 .

The difference, $|z'_0 - z_0|$, from one iteration can sometimes be impacted by random round-off noise, rather than the dynamical systems themselves as desired. On the other hand, if chaos is sufficiently weak, the difference is still invisible by just one-time scaling. Therefore, to overcome this difficulty, it may be necessary to implement multiple iterations, $z_0 \xrightarrow{f^N} z_N \xrightarrow{f^{-N}} z'_0$, ($N \geq 2$). The difference can be estimated similarly as Eq. (7),

$$(z'_0 - z_0)_N \approx \sum_{n=1}^N \Delta z_n \prod_{j=0}^{n-1} \left[\frac{df}{dz} \Big|_{z=f^j(z_0)} \right]^{-1} + \sum_{n=1}^N \Delta z'_n \prod_{j=0}^{n-2} \left[\frac{df}{dz} \Big|_{z=f^j(z_0)} \right]^{-1}. \quad (9)$$

Here f^j represents forward j -iterations and f^{-j} represents reverse j -iterations. Eq. (9) illustrates that round-off errors are cumulative for each iteration and are scaled by local linear matrices along the trajectories in both directions. With sufficient iterations, the cumulative difference indicates the chaos of the trajectory.

It is worth noting that, even if a system has no chaos, the cumulative random error between forward integration and its corresponding reversal is directly proportional to the number of iterations executed [25]. If chaos is present, however, the error will grow much faster.

In large scale modern accelerators, F-R integrations need to be evaluated magnet-by-magnet. A full-cycle around an accelerator equates to one iteration as described above. The round-off errors Δz receive a contribution from each integration step. A short-term tracking simulation could generate an observable difference when 64 bit floating numbers were used. To be specific, only one-turn F-R integrations were used to optimize the DA of the NSLS-II storage ring. Usually these differences are observable but still at quite small scale, therefore a base-ten logarithm is used to allow a large range to better represent them,

$$\Delta_s = \log_{10} |z_0 - z'_0|. \quad (10)$$

In principle, a relative difference $|\Delta z|/|z|$ should be used as the chaos indicator [24]. During optimization implementation, the desired DA region is divided into many zones (see Sect. IV B). In each zone, the absolute coordinate values are limited to a narrow range. Therefore, to save computation time and expedite the optimization, an absolute difference is used for this method.

III. HÉNON MAP

In this section, the F-R integration method is used to study a 1-dimensional Hénon map,

$$\begin{pmatrix} x \\ p \end{pmatrix}_n = \begin{pmatrix} \cos \mu & \sin \mu \\ -\sin \mu & \cos \mu \end{pmatrix} \begin{pmatrix} x \\ p - x^2 \end{pmatrix}_{n-1}. \quad (11)$$

This discrete Hénon map represents a thin-lens sextupole kick followed by a linear phase space rotation at a phase advance μ . Its reversal map can be expressed first, in the inverse rotation, and then followed by the inverse thin-lens kick,

$$\begin{pmatrix} x_t \\ p_t \end{pmatrix} = \begin{pmatrix} \cos \mu & -\sin \mu \\ \sin \mu & \cos \mu \end{pmatrix} \begin{pmatrix} x \\ p \end{pmatrix}_n, \quad \begin{pmatrix} x \\ p \end{pmatrix}_{n-1} = \begin{pmatrix} x_t \\ p_t + x_t^2 \end{pmatrix}, \quad (12)$$

where x_t, p_t are the intermediate variables.

The Hénon map's linear phase advance is chosen as $\mu = 0.205 \times 2\pi$ in order to observe the 5th-order resonance line. The difference between initial conditions obtained from the F-R integration is illustrated in Fig. 2. When the F-R integrations are calculated with only 10-50 iterations (as shown in the top row), the area of the stable region are overestimated and the inside resonances are almost invisible. After 100 iterations, the resonance lines and stable islands become gradually visible. More iterations can provide much more detailed chaos information as illustrated in the two bottom subplots.

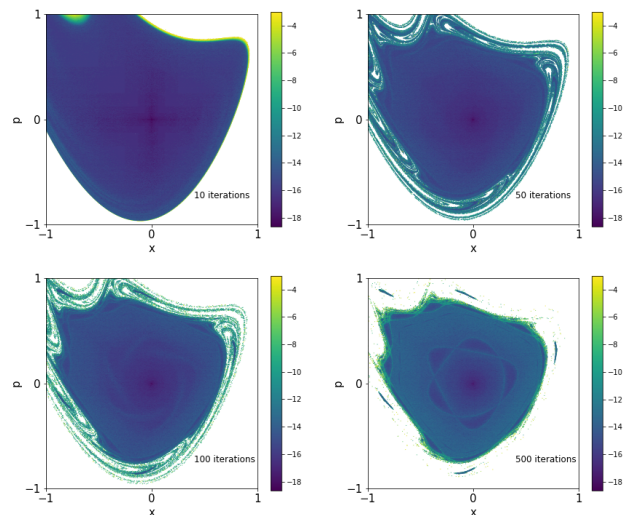


Figure 2. (Colored) Contour of the F-R integrations with different numbers of iterations for a Hénon map. The colormap represents the difference of initial conditions as a function of the phase space coordinates x - p . More iterations provide more detailed chaos information, but even with just a few dozen iterations, an early indicator of chaos can be determined.

IV. APPLICATIONS

In this section we demonstrate this method by optimizing the dynamic apertures for the National Synchrotron Light Source II (NSLS-II) [26] main storage ring and a test diffraction-limited light source ring.

A. NSLS-II storage ring

NSLS-II is a dedicated 3rd generation medium energy (3GeV) light source operated by Brookhaven National Laboratory. Its main storage ring's lattice is a typical double-bend-achromat structure. Its linear optics for one cell is illustrated in Fig. 3. The whole ring is composed to +2 by three families of chromatic sextupoles inside dispersive achromats. The optimization knobs are six families of harmonic sextupoles located at dispersion-free sections. The goal of optimization is to obtain a sufficient DA ($|x| > 15mm, |y| > 5mm$) for the off-axis injection at the long straight section center, and a $|\delta| > 2.5\%$ momentum acceptance to ensure a 3 hour lifetime at a 500 mA beam current.

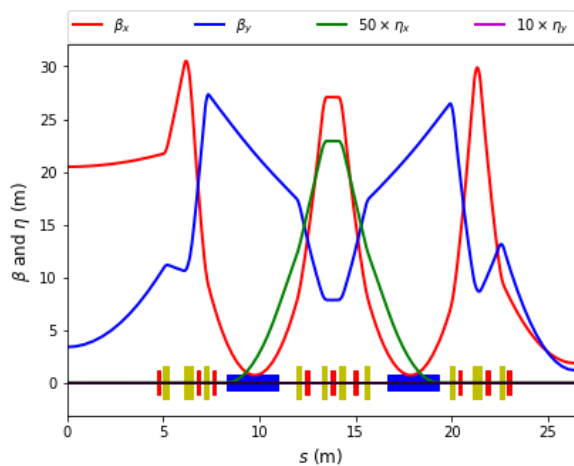


Figure 3. (Colored) The linear optics and magnet layout for one of the 30 cells of the NSLS-II storage ring. The red blocks represent sextupoles. The three located between two dipoles are used to correct the natural chromaticity. The remaining six are used here for DA optimization.

B. Optimization objectives and results

On the transverse x - y plane at the injection point, multiple initial conditions are uniformly populated within a Region Of Interest (ROI). The ROI is chosen to cover the needed aperture. The virtual particle trajectories are simulated with a 4th order kick-drift symplectic integrator [27]. The symplectic integration is implemented with a python code, which has been independently benchmarked with another reliable tracking simulation code IMPACTZ [28]. After evolving some revolutionary periods (usually an integer number of turns), their reversal trajectories are computed by switching the sign of the coordinate s and letting particles run back to $s = 0$. Newly re-established initial conditions deviate from the original ones. A large difference between a pair of initial condi-

tions indicate a stronger chaos. The goal of optimization then becomes minimizing the difference for all pairs of initial conditions within the ROI. It is not practical or necessary to minimize so many pairs of initial conditions simultaneously, therefore, the ROI is divided into several zones as shown in Fig. 4. For each zone, the difference of initial conditions are averaged over all F-R integrations pairs. Then the averaged values for all zones are used as the optimization objectives, which need to be minimized simultaneously to suppress the chaos inside the whole ROI. The optimization objective functions f reads as

$$\bar{\Delta}_i = f_i(K_{2,j}), \quad (13)$$

where, i, j are the indices of the ROI zones and the sextupoles respectively, $\bar{\Delta}_i$ is the average difference in the i^{th} zone, and K_2 are the the optimization knobs, i.e. normalized sextupole gradients.

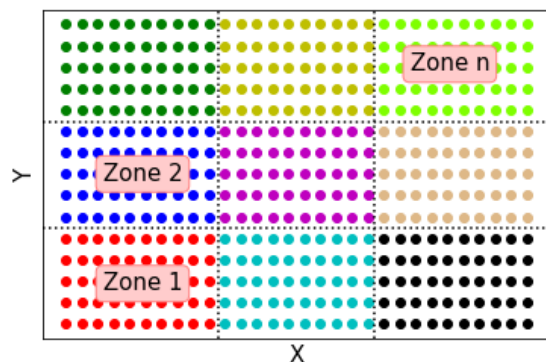


Figure 4. (Colored) Dividing the region of interest (ROI) into n zones in the x - y plane. In each zone, multiple initial conditions (represented with same-colored dots) are uniformly populated. The optimization objectives are the difference between the initial conditions of F-R integrations averaged over each zone.

Quantitatively, the difference in Eq. (10) and (13) for a pair of initial conditions in the normalized phase space can be computed as

$$\Delta = \log_{10} \sqrt{\Delta \bar{x}^2 + \Delta \bar{p}_x^2 + \Delta \bar{y}^2 + \Delta \bar{p}_y^2}, \quad (14)$$

where $u = x$, or y , $\Delta \bar{u}$ and $\Delta \bar{p}_u$ are the difference of canonical coordinates normalized with Courant-Snyder parameters α_u and β_u as follows [29],

$$\begin{bmatrix} \Delta \bar{u} \\ \Delta \bar{p}_u \end{bmatrix} = \begin{bmatrix} \frac{1}{\sqrt{\beta_u}} & 0 \\ \frac{\alpha_u}{\sqrt{\beta_u}} & \sqrt{\beta_u} \end{bmatrix} \begin{bmatrix} \Delta u \\ \Delta p_u \end{bmatrix}. \quad (15)$$

The normalization of Eq. (15) expresses the canonical coordinate pairs in the same units \sqrt{m} for arithmetic addition.

To obtain sufficient beam lifetime and DA simultaneously, one must optimize them simultaneously [30].

Direct optimization of beam lifetime through local momentum acceptance, however, is time-consuming. An alternative method is to calculate several different off-momentum DA and optimize them with the on-momentum DA, in parallel. This was achieved by a δ -slicing method as illustrated in Fig. 5. First, the desired energy acceptance range is determined based on the beam scattering lifetime at a certain beam current. Then several sliced off-momentum DA are included. At each slice, several zones' objective functions are evaluated separately.

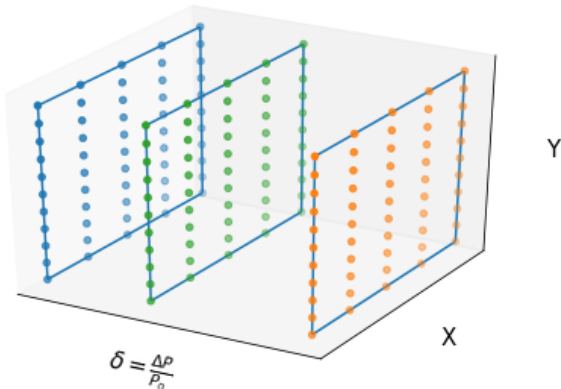


Figure 5. (Colored) Optimizing several fixed off-momentum DA simultaneously. By separating a 5-dimensional phase space $(x, p_x; y, p_y; \delta)$ into several slices along the δ -axis, DA for off-momentum particles can be optimized simultaneously.

Multiple zones within the ROI for different momentum slices need be minimized simultaneously. The multi-objective genetic algorithm (MOGA) was used for this task. More turns of particle tracking simulation can indicate the chaos more accurately, but this requires more computation time. To boost the optimization, only one-turn F-R integrations (crossing 30 cells) were computed as illustrated in Fig. 6. Although the early indicator of chaos provides an optimistic approximation, it does rule out many of the less competitive candidates and narrows down the parameter search ranges quickly. By allowing a small scale population, which includes the evolution of only 1,000 candidates over just 50 generations, the top candidates' average fitness is seen to converge. It took about 6 hours to complete the optimization with 50 Intel® Xeon® 2.2-2.3 GHz CPU cores. Another reliable tracking code ELEGANT [31] was then used to check the DA for all the candidates only inside the last generation. Among them, some of the elite candidates are selected for more extensive simulation studies to check their final performance.

The DA profiles for the top 100 candidates inside the last generation are illustrated in Fig. 7. Although the six sextupole settings are very different, their DA satisfy the minimum requirement for top-off injection. This observation confirms that short-term F-R integration can

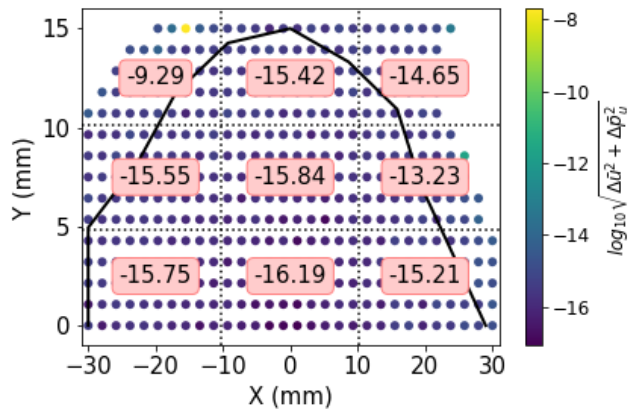


Figure 6. (Colored) The $\delta = 0$ slice's 9 zones' objective values. As shown in the boxes, these were obtained from one-turn F-R integrations for a specific set of sextupoles settings at the NSLS-II storage ring. Blank points represent lost particles during the tracking. The maximum allowed number of lost particles is used as an optimization constraint. The black line is the dynamic aperture obtained by multi-turn (1,024) tracking simulation with the code ELEGANT. The one-turn F-R integrations give a more optimistic result than the multi-turn tracking simulation. As an early indicator of chaos, however, it does provide a reasonable criteria for the optimizer.

indeed be used for DA optimization. Among these candidates, one from the elite cluster was selected to carry out a more detailed frequency map analysis (FMA) to verify its nonlinear dynamics performance. The FMA results are summarized later in Sect. IV C.

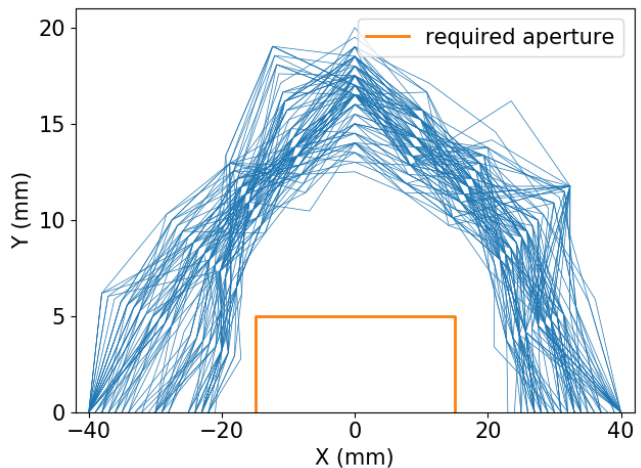


Figure 7. (Colored) DA of the top 100 candidates (measured with the area) from the 50th generation of the evolved population obtained with the MOGA optimizer. The light yellow box is the required aperture for the off-axis top-off injection.

In the specific example of a dedicated light source machine (the NSLS-II storage ring), the longitudinal synchrotron oscillation has not been included. It is straight-

forward to include it if needed. It can be done by extending Eq. (14) to the 6-dimensional space when the betatron-synchrotron coupling resonances become critically important, e.g. in the case of collider rings.

C. Comparison with frequency map analysis

Frequency map analysis (FMA) is widely used to evaluate the performance of a nonlinear lattice [32?–34]. FMA was also applied directly to optimizing the DA of a light source ring [35]. By comparing the tune diffusion rate determined by two pieces of turn-by-turn simulation or measurement data, the resonances of the lattice can be visualized. In our example, one elite solution was selected from the last generation of candidates to carry out a detailed FMA to characterize its nonlinear dynamics performance. In the meantime, a multi-turn (1,024 turns) F-R analysis was conducted for a comparison with the FMA results. The sextupole settings for the current NSLS-II lattice and the select elite solution are listed in Tab. I for comparison.

Table I. Comparison of two sextupoles settings

Sextupole	unit	K_2 (current)	K_2 (F-R)
SH1	m^{-3}	19.8329	19.8495
SH3	m^{-3}	-5.8551	-0.4017
SH4	m^{-3}	-15.8209	-22.0160
SL3	m^{-3}	-29.4609	-29.0057
SL2	m^{-3}	35.6779	27.9185
SL1	m^{-3}	-13.2716	-2.6051

Fig. 8 illustrates the comparison of the on-momentum DA in the transverse x - y plane. Fig. 9 shows the comparison of the off-momentum acceptance in the x - δ plane. When comparing the two figures, the FMA results yield more copious and fine patterns of the chaos indicator. However, the resolution of the FMA is sensitive to the accuracy of measurement of the frequencies. Much of the fine patterns of the FMA may not be from real chaotic orbits. For example, consider an orbit whose fundamental frequencies and their harmonics having similar amplitudes that are mixed together. In this case, a small fluctuation in amplitude of those frequencies over a separate period of data acquisition could result in differently ordered frequencies in the Numerical Analysis of Fundamental Frequencies (NAFF) algorithm [33]. As for other cases, when orbital frequencies are relatively close to the data sampling rate, compared to the inverse of the number of the sample, the measured frequency can fluctuate as the time windows shift [36]. In general, these incorrect fine patterns fade away as longer sampling time is used to improve the accuracy of the frequency measurement [14]. However, the speed of improvement of the accuracy of the NAFF is proportional to the inverse power [37] of the sampling time. It is relatively slow compared to the

exponential improvement of the reversal method.

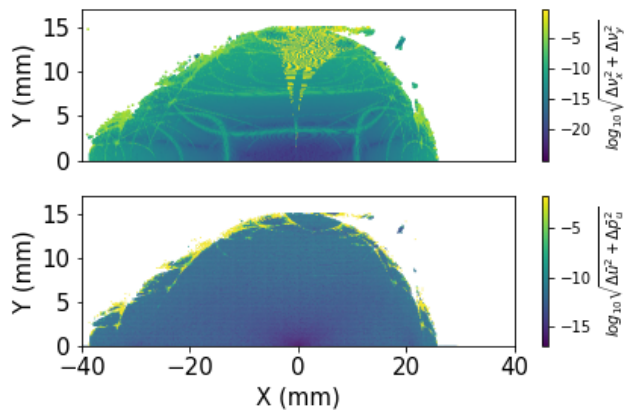


Figure 8. (Colored) Top: FMA on the x - y plane for 1,024 turns of data (512 leading and 512 trailing turns) with the code ELEGANT. Bottom: F-R analysis for 1,024 turns. Using the FMA, some unusual diffusion rate (as shown in yellow stripe near $x = 0$) can be observed. This is most likely due to incorrect tune peaks picked up from the tune spectrums in the NAFF algorithm.

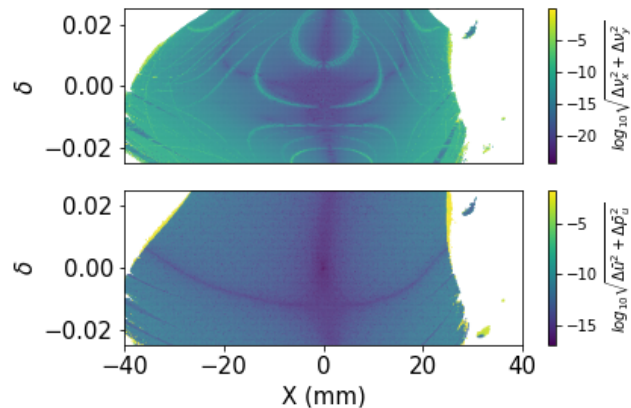


Figure 9. (Colored) Top: FMA on the x - δ plane for 1,024 turns of data (512 leading and 512 trailing turns) with the code ELEGANT. Bottom: F-R analysis for 1,024 turns.

Control of higher order chromaticities and amplitude-dependent-tune-shifts to avoid destructive resonance-crossing is critical in DA optimization. This can be achieved by minimizing some specific nonlinear driving terms [38, 39]. For example, $C_{2200,0}$, $C_{0022,0}$, $C_{1111,0}$ are the first order amplitude-dependent-tune-shift coefficients; then $C_{1100,n}$, $C_{0011,n}$, $n \geq 2$ are the higher order chromaticity coefficients. These terms can be used as either objective functions or explicit constraints. In the F-R integration method, no explicit constraints are used to limit them. The final tracking simulation on the selected solution, however, shows that both the amplitude-dependent-tune-shifts (Fig. 10) and the higher order

chromaticities (Fig. 11) are automatically and passively suppressed. The on-momentum and two off-momentum ($\pm 2.5\%$) DA, computed with the code ELEGANT, are shown in Fig. 12.

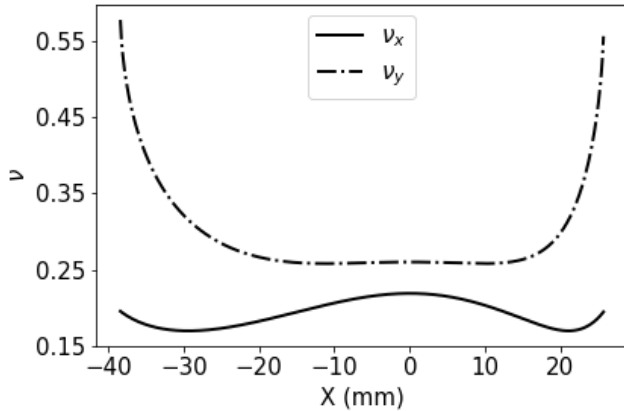


Figure 10. Tune shift with amplitude in the horizontal plane for the selected candidate. Although the vertical tune rises suddenly faster at larger horizontal amplitudes, the tune variations are within ± 0.03 inside the range of $x \in [-15, 15]$ mm.

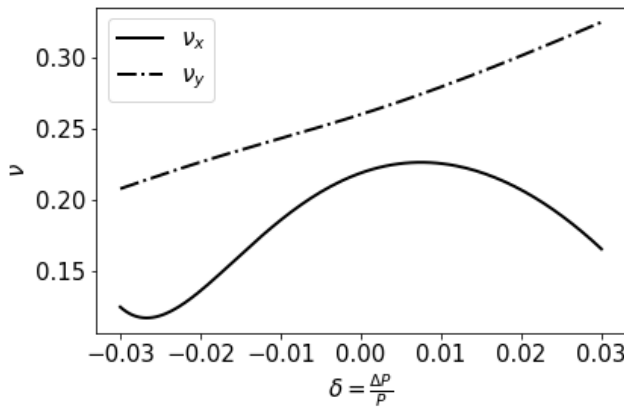


Figure 11. Tune variation with the momentum offset, i.e. chromaticity for the selected candidate. The linear chromaticities were tuned to +2 for both x and y planes.

The optimization was implemented on an error-free model. Then the systematic and random magnetic field errors and the misalignments have been included to confirm the robustness of the solution. An online beam test on the NSLS-II storage ring was also carried out to confirm that the off-axis top-off injection efficiency is close to 100%. The beam lifetime at a 400 mA beam current is longer than 5.5 hours, with a diffraction-limited vertical beam emittance of $8 \text{ pm} \cdot \text{rad}$.

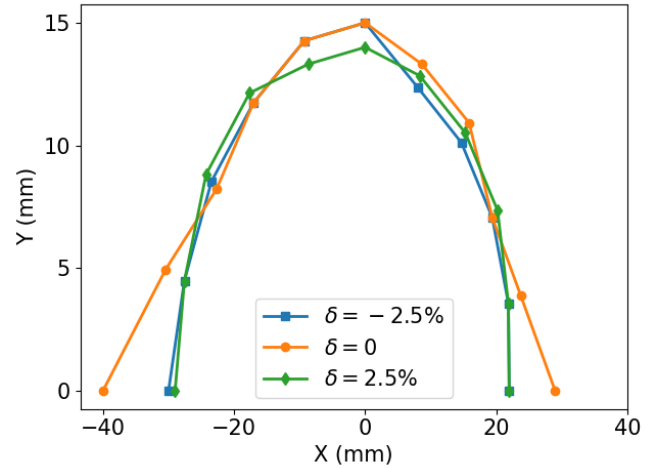


Figure 12. (colored) On- and two off-momentum DA for the selected candidate.

D. MBA lattice for diffraction-limited light source

The F-R integration method has also been used to test on a multi-bend-achromat (MBA) structure, which could potentially be used as a diffraction-limited light source storage ring lattice in the future. The horizontal emittance of the test MBA lattice used was $78 \text{ pm} \cdot \text{rad}$ at a beam energy of 2 GeV. The linear lattice is shown in Fig. 13, in which most sextupoles are chromatic sextupoles. The MOGA result showing the top 100 candidate apertures is illustrated in Fig. 14. The preliminary result confirms that the F-R integration could also be applied to a more complicated nonlinear lattice, and the approach itself should be general in optimizing other lattices.

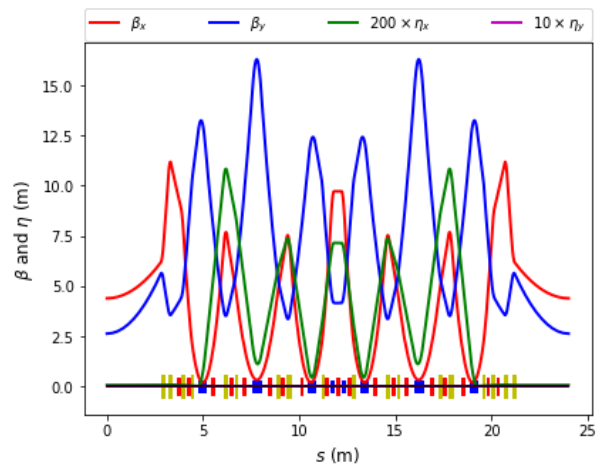


Figure 13. (Colored) Linear optics and magnet layout for one cell of a test MBA lattice.

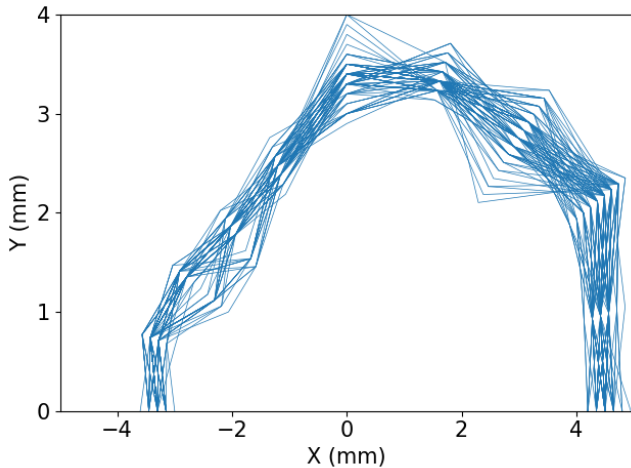


Figure 14. (Colored) On-momentum DA for the top 100 candidates for the test MBA lattice.

V. SUMMARY

An indicator of chaos obtained with forward-reversal integration has been used for optimization of dynamic aperture of storage rings. The indicator, intrinsically but empirically associated with the Lyapunov exponent, gives an early indication of the chaos of beam motion in storage rings. Although the indicator can not give the exact dynamic aperture profile with a short-term tracking simulation, a concrete correlation and large MOGA

candidate pool yields some optimal lattice solutions. The NSLS-II storage ring and a test MBA lattice are used as examples to illustrate the application of this method.

ACKNOWLEDGMENTS

We would like to thank C. Mitchell and R. Ryne (LBL) for the stimulating and collaborative discussions, J. Qiang (LBL) for providing the code IMPACTZ, Z. Bai (USTC) for providing the test MBA lattice, M. Giovannozzi (CERN) for fruitful discussion and constructive suggestion, M. Borland (ANL) for implementing this method in the ELEGANT code, and I. Morozov (BINP) for pointing out a numerical error in the manuscript. This research used resources of the National Synchrotron Light Source II, a U.S. Department of Energy (DOE) Office of Science User Facility operated for the DOE Office of Science by Brookhaven National Laboratory (BNL) under Contract No. DE-SC0012704, and the computer resources at the National Energy Research Scientific Computing Center. This work was also supported by (1) the Accelerator Stewardship program under the Office of High Energy Physics; (2) the Director, Office of Science of the U.S. DOE by Lawrence Berkeley National Laboratory under Contract No. DE-AC02-05CH11231, (3) BNL Laboratory Directed Research and Development program “NSLS-II High Brightness Upgrade and Design Studies” No. 17-015. (4) DOE SBIR grant under Contract No. DE-SC0019538. One author (KH) acknowledges the support from the U.S. DOE Early Career Research Program under the Office of High Energy Physics.

-
- [1] F. Zimmermann, “Comparison of calculated with measured dynamic aperture,” *4th European Particle Accelerator Conference (EPAC 94) London, England, June 27-July 1, 1994*, Conf. Proc. **C940627**, 327–331 (1994).
 - [2] Salman Habib and Robert D. Ryne, “Symplectic calculation of lyapunov exponents,” *Phys. Rev. Lett.* **74**, 70–73 (1995).
 - [3] W. Scandale, “Dynamic aperture,” *Accelerator physics at the Superconducting Super Collider. Lectures held at the Central Facility auditorium of the SSC Laboratory, Waxahachie, TX, Oct 1, 1992 to Sep 30, 1993*, AIP Conf. Proc. **326**, 52–97 (1995), [52(1997)].
 - [4] M. Giovannozzi, W. Scandale, and E. Todesco, “Inverse logarithm decay of long term dynamic aperture in hadron colliders,” in *17th IEEE Particle Accelerator Conference (PAC 97): Accelerator Science, Technology and Applications Vancouver, British Columbia, Canada, May 12-16, 1997* (1997).
 - [5] M. Giovannozzi, W. Scandale, and E. Todesco, “Dynamic aperture extrapolation in presence of tune modulation,” *Phys. Rev.* **E57**, 3432–3443 (1998).
 - [6] Alan Wolf, Jack B. Swift, Harry L. Swinney, and John A. Vastano, “Determining lyapunov exponents from a time series,” *Physica D: Nonlinear Phenomena* **16**, 285 – 317 (1985).
 - [7] F. T. Cole, “Oh Camelot!: A memoir of the MURA years,” (1994).
 - [8] R. H. Miller, “Irreversibility in Small Stellar Dynamical Systems.” *Astrophys. J.* **140**, 250 (1964).
 - [9] R Genesio and A Vicino, “New techniques for constructing asymptotic stability regions for nonlinear systems,” *IEEE transactions on circuits and systems* **31**, 574–581 (1984).
 - [10] H-D Chiang, Morris W Hirsch, and Felix Fulih Wu, “Stability regions of nonlinear autonomous dynamical systems,” *IEEE Transactions on Automatic Control* **33**, 16–27 (1988).
 - [11] Mia Loccufier and Erik Noldus, “A new trajectory reversing method for estimating stability regions of autonomous nonlinear systems,” *Nonlinear dynamics* **21**, 265–288 (2000).
 - [12] Hsiang-Kung Lee and Kuang-Wei Han, “Analysis of nonlinear reactor systems by forward and backward integration methods,” *IEEE Transactions on Nuclear Science* **47**, 2693–2698 (2000).
 - [13] Luc Jaulin, Isabelle Braems, Michel Kieffer, and Eric Walter, “Nonlinear state estimation using forward-backward propagation of intervals in an algorithm,” in

- Scientific computing, validated numerics, interval methods* (Springer, 2001) pp. 191–201.
- [14] Kilean Hwang, Chad Mitchell, and Robert Ryne, “Chaos Indicators for Studying Dynamic Aperture in the IOTA Ring with Protons,” in *Proceedings, 10th International Particle Accelerator Conference (IPAC2019): Melbourne, Australia, May 19-24, 2019* (2019) p. WEPTS078.
- [15] Kalyanmoy Deb, *Multi-Objective Optimization Using Evolutionary Algorithms* (Wiley, 2001).
- [16] Lingyun Yang, David Robin, Fernando Sannibale, Christoph Steier, and Weishi Wan, “Global optimization of an accelerator lattice using multiobjective genetic algorithms,” *Nuclear Instruments and Methods in Physics Research Section A: Accelerators, Spectrometers, Detectors and Associated Equipment* **609**, 50 – 57 (2009).
- [17] Lingyun Yang, Yongjun Li, Weiming Guo, and Samuel Krinsky, “Multiobjective optimization of dynamic aperture,” *Phys. Rev. ST Accel. Beams* **14**, 054001 (2011).
- [18] Yongjun Li and Lingyun Yang, “Multi-objective dynamic aperture optimization for storage rings,” *Proceedings, HKUST Jockey Club Institute for Advanced Study: The Future of High Energy Physics (HKUST): Hong Kong, China, January 18-21, 2016*, *Int. J. Mod. Phys. A* **31**, 1644019 (2016).
- [19] Yongjun Li, Weixing Cheng, Li Hua Yu, and Robert Rainer, “Genetic algorithm enhanced by machine learning in dynamic aperture optimization,” *Phys. Rev. Accel. Beams* **21**, 054601 (2018).
- [20] Jinyu Wan, Paul Chu, Yi Jiao, and Yongjun Li, “Improvement of machine learning enhanced genetic algorithm for nonlinear beam dynamics optimization,” *Nuclear Instruments and Methods in Physics Research Section A: Accelerators, Spectrometers, Detectors and Associated Equipment* **946**, 162683 (2019).
- [21] A. Liu, A. Bross, and D. Neuffer, “Optimization of the magnetic horn for the nuSTORM non-conventional neutrino beam using the genetic algorithm,” *Nuclear Instruments and Methods in Physics Research Section A: Accelerators, Spectrometers, Detectors and Associated Equipment* **794**, 200 – 205 (2015).
- [22] A. Liu, A. Bross, and D. Neuffer, “A FODO racetrack ring for nuSTORM: design and optimization,” *Journal of Instrumentation* **12**, P07018–P07018 (2017).
- [23] G. Ripken, “Nonlinear canonical equations of coupled synchrotron motion and their solution within the framework of a nonlinear six-dimensional (symplectic) tracking program for ultrarelativistic protons,” (1985).
- [24] IEEE 754 Committee, *IEEE Standard for Floating-Point Arithmetic*, Tech. Rep. 754-2019 (Microprocessor Standards Committee of the IEEE Computer Society, New York, NY, 2019).
- [25] Jackson Laslett, “Round-Off Errors From Fixed-Point Linear Algebraic Transformations Computer by IBM-704 Program 117,” (1957).
- [26] BNL, <https://www.bnl.gov/ns1s2/project/PDR/>.
- [27] H. Yoshida, “Construction of higher order symplectic integrators,” *Phys. Lett.* **A150**, 262–268 (1990).
- [28] Ji Qiang, Robert D. Ryne, Salman Habib, and Viktor Decyk, “An object-oriented parallel particle-in-cell code for beam dynamics simulation in linear accelerators,” *Journal of Computational Physics* **163**, 434 – 451 (2000).
- [29] E.D Courant and H.S Snyder, “Theory of the alternating-gradient synchrotron,” *Annals of Physics* **3**, 1 – 48 (1958).
- [30] M. Borland, L. Emery, V. Sajaev, and A. Xiao, “Multi-objective Optimization of a Lattice for Potential Upgrade of the Advanced Photon Source,” *Conf.Proc. C110328*, 2354–2356 (2011).
- [31] M. Borland, “elegant: A Flexible SDDS-Compliant Code for Accelerator Simulation,” in *6th International Computational Accelerator Physics Conference (ICAP 2000) Darmstadt, Germany, September 11-14, 2000* (2000).
- [32] D. Robin, C. Steier, J. Laskar, and L. Nadolski, “Global Dynamics of the Advanced Light Source Revealed through Experimental Frequency Map Analysis,” *Phys. Rev. Lett.* **85**, 558–561 (2000).
- [33] J. Laskar, “Frequency Map Analysis and Particle Accelerators,” in *20th Particle Accelerator Conference (PAC 03)* (2003) p. 378.
- [34] Yannis Papaphilippou, “Detecting chaos in particle accelerators through the frequency map analysis method,” *Chaos: An Interdisciplinary Journal of Nonlinear Science* **24**, 024412 (2014), <https://doi.org/10.1063/1.4884495>.
- [35] Christoph Steier and Weishi Wan, “Quantitative lattice optimization using frequency map analysis,” *Proc. of IPAC*, 4746–4748 (2010).
- [36] A Valishev, S Nagaitsev, D Shatilov, and V Danilov, “Beam physics of integrable optics test accelerator at fermilab,” in *2012 International Particle Accelerator Conference* (2012) p. 1371.
- [37] Jacques Laskar, “Introduction to frequency map analysis. in: Simó C. (eds) Hamiltonian systems with three or more degrees of freedom. NATO ASI Series (Series C: Mathematical and physical sciences),” (Springer, Dordrecht, 1999) pp. 134–150.
- [38] Alex J. Dragt, *Lie methods for nonlinear dynamics with applications to accelerator physics* (Unpublished, 2011).
- [39] Alex Chao, *Lecture notes on topics in accelerator physics* (Unpublished, 2002).